Thermal monitoring of LiFePO4 batteries using switching harmonics

Cristina Gonzalez Moral[††], Daniel Fernandez[†], Juan Manuel Guerrero[†], David Reigosa[†], Carlos Rivas[††] and Fernando Briz[†]

† University of Oviedo. Dept. of Elect. Computer & System Engineering, Gijón, 33204, Spain.

† † Electrotécnica Industrial y Naval, S.L. (ELINSA), 15008, A Coruña, Spain

cgonzalez@elinsa.org, fernandezalodaniel@uniovi.es, guerrero@uniovi.es, diazdavid@uniovi.es, crivas@elinsa.org, fernando@isa.uniovi.es

Abstract: Thermal monitoring is of high relevance for safe operation and degradation management of batteries. Direct measurement of battery temperature has drawbacks due to both cost and reliability issues. To overcome these limitations, the development of temperature estimation methods has received significant research attention. Most of the existing estimation methods are based in the injection of an additional signal, which can produce additional losses. This paper proposes a temperature estimation method for LiFePO4 batteries using the switching harmonics of the converter feeding the battery. Temperature changes are estimated from the variation of the battery impedance at the switching frequency. The method operates online and without interfering with the normal operation of battery and power converter, and does not introduce therefore additional losses or any other adverse effect in the batteries.[1]

Index Terms — $LiFePO_4$ batteries, thermal monitoring, temperature estimation, impedance estimation.

I. Introduction

The use of energy storage systems (ESS) based on batteries has dramatically increased during the last two decades [1]. A wide variety of systems such as microgrids [2]-[4], electric vehicles (EV) [5]-[9] or aerospace applications [10]-[12] use batteries ESS, with energy/power requirements strongly depending on the application [12]. Development of battery monitoring methods aimed to guarantee safe operation and to improve their performance, reliability and lifetime, being the focus of significant research efforts [4], [12]-[14].

Batteries can be classified as primary (not rechargeable) and secondary (rechargeable). Examples of primary batteries are zinc-carbon (zinc chloride), magnesium/manganese dioxide (Mg/MnO_2) or alkaline-manganese dioxide (zinc /KOH/MnO_2). Examples of secondary batteries are lead-acid, nickel-cadmium (NiCd), nickel-metal hydride (NiMH), lithium-ion (Li-ion) or Li-ion-polymer [15]. Lithium-Ion Batteries (LIBs) are the most common choice in high capacity ESS, often used in microgrids [1], [16], electric vehicles (EV) [6]-[7], [9] or satellites [12], [17], applications. Batteries consist of three main elements: anode, cathode, and electrolyte. Graphite is the most common anode choice in LIBs. LIB cathode materials are usually oxides, as lithium-cobalt oxide ($LiCoO_2$ or LCO), lithium- manganese oxides ($LiMn_2O_4$ or LMO) or lithium iron phosphate ($LiFePO_4$ or LFP). In addition, the separator between cathode and anode prevents both of them to react directly in the electrolyte [1], [18], [19]. The negative current collector is made of copper and the positive current collector is made of aluminum [1].

Among LIBs, $LiFePO_4$ batteries are the third most used type and keep a similar market growth rate to their counterparts [20]. The reasons for this are their advantages in terms of safety, low toxicity (in opposition to cathodes based on rare metal composites, as LCO [21]), long cycle life (>2000), high power capability, reliability, relatively low cost, wide temperature range (-20ºC – 60ºC) and flat voltage profile (considered as a drawback from the point of view of SOC estimation [21]). As a drawback, compared to other LIBs, they have low-average cell voltage (3.2V) and lower specific energy (90–120Wh/kg) [6], [18]-[22].

LIBs are very sensitive to temperature variations; e.g. Open-Circuit Voltage (OCV), capacity or its internal resistance [9], [23]-[25], have been reported to be affected. Furthermore, operating temperature limits can be different during charging and discharging processes [26]. While higher battery temperature may temporarily increase its capacity, it also increases the internal resistance in the long term, due to premature aging. This increases the losses and the risk of thermal runaways, fires, and explosions [1], [27]-[30]. Over 80ºC, thermal runaway can occur spontaneously due to the exothermic reactions taking place between electrolyte, anode, and cathode, which can cause the decomposition of the solid-electrolyte interphase (SEI), electrolyte and/or electrodes [27], [28]. This temperature may vary depending on the battery constructive elements, as the electrolyte solvents [29]. On the other hand, lower temperatures result in a reduction of the power and energy capabilities as the diffusion of the lithium in the electrolyte is reduced [30], [31]. A $LiFePO_4$ battery as the one in [26] can operate between -20ºC and 60ºC while discharging, but only from -10ºC to 45ºC while charging. It is concluded from the previous discussion that LIB temperature monitoring is of great importance, which explains the proliferation of temperature measurement [6], [9], [30] and estimation [28], [29], [32]-[40] methods during the last decade.

[1] This work was supported in part by the Research, Technological Development and Innovation Programs of the Spanish Ministry Economy and Competitiveness, under grant MINECO-17-ENE2016-80047-R, by the Oviedo Siembra Talento program of the Oviedo City Council, by the FEDER INTER-CONNECTA 2015 program under grant ITC20151130 and by the Government of Asturias under project IDI/2018/000188 and FEDER funds.

LIB temperature can be directly measured using temperature sensors [32], as RTD (Resistance Temperature Detector) [33], like a PT100 [6], or thermocouples [30], [34], [35]. While the sensors themselves can be cheap, their installation and the subsequent cabling, signal conditioning and acquisition, add cost and complexity and can compromise the system reliability as there are more elements susceptible to failure. In addition, determining the number and location of the sensors to trade-off accuracy, cost, and complexity, is not straightforward.

Alternatively, LIB temperature can be estimated [28], [29], [32]-[40]. Estimation methods rely on the relationship between the battery impedance and its temperature. The battery impedance is typically estimated by injecting sinusoidal currents, which are preferably injected when the battery is at rest to improve the accuracy; however, this limits the applicability of the method; as an alternative, methods based on the impedance estimation while the battery is at use has been recently proposed [41].

This paper proposes temperature estimation for $LiFePO_4$ batteries using the switching harmonics produced by the converter interfacing the battery [42]. Temperature is estimated from the measured battery impedance at the switching frequency. The proposed method avoids injection of additional signals and does not interfere with the normal operation of the battery.

The paper is organized as follows: the electrical modeling of batteries is discussed in section III; the variation of battery voltage with the State Of Charge (SOC) and the consequent need for a converter is studied in section IV; the proposed battery temperature estimation method using switching harmonics is presented in section V; implementation issues are discussed in section VI; experimental results are shown in section VII; conclusions are finally presented in section VIII.

II. Temperature estimation of LIB

This section briefly reviews existing LIB temperature estimation methods. In [29] and [36] phase shift between applied sinusoidal current and the resulting voltage at 40 Hz was presented as a reliable metric of internal cell temperature. This method was further analyzed in [37] concluding that SOC affects low-frequency impedance. Impedance measurement was performed at higher frequencies, i.e. 10.3 kHz, to avoid SOC influence. In [33] the phase shift between voltage and current for temperature estimation was also used, including SOC correction for more precise estimation. In [34] frequency selection to minimize the interference of SOC and SOH (State-of-Health) for LIBs was analyzed. The temperature of a lithium-ion battery is estimated by analyzing the impedance phase and magnitude change with temperature. Depending on the temperature, the frequency range used to estimate the temperature without being influenced by the SOC changes. The lowest frequency that can be used is almost independent of temperature, while the highest one significantly changes; especially challenging is the operation at low temperatures (-10ºC). This study also concludes that SOH has almost no effect on the phase angle of the battery impedance. The conclusion regarding frequency range selection for temperature estimation (1-100 Hz) slightly differs from those in [32], a potential reason being the differences in LIB technologies used in each study. This study was further extended in [35] adding a thermocouple to the battery to improve the temperature estimation. In [38], the zero-intercept frequency (ZIF), which is the frequency at which the impedance seen in the EIS plot crosses the real axis, was shown to be dependent solely on the cell temperature, not being affected by SOC and aging. This work was further developed in [39], where a so-called non-zero intercept frequency, a frequency in which the imaginary part of the impedance is equal to a non-zero constant, is used to estimate battery temperature. The constant is selected depending on the application and allows the selection of a range of frequencies which is not affected by disturbing frequencies that can interfere with the injected frequencies. Resulting estimations are shown to be better than in [35] because of its higher signal-to-noise ratio. In [32], a combination of impedance estimation based on voltage and current measurements and surface cell temperature measurements was presented to estimate the internal temperature in cylindrical $LiFePO_4$ batteries. The battery was excited with a current at 215 Hz for this purpose, this frequency was shown (see also [29] and [36]) to be high enough to be SOC independent. In [28], a frequency of 300 Hz is used. At this frequency, a strong temperature dependency was found in the battery impedance with a low dependence from the SOC. The Arrhenius model is reported to fail in correctly estimating temperatures above 68ºC; additional models are, therefore, proposed for higher temperatures. The method presented in [32] was improved in [40] by avoiding cell temperature measurements. Impedance estimation at 215 Hz and an extended Kalman filter (EKF) were combined instead. However, a calibration measurement must be still carried out with the battery at rest.

III. Electrical modeling of batteries

Several electric equivalent-circuits have been proposed to model the electrical behavior of batteries, including Thévenin [7], [21], [43], RC [7], [43], [44], and Randles (impedance-based) [10], [28], [43], [45], [46] models. These models are simpler (i.e. with lower computational burden) alternatives to chemical and mathematical models often based on partial differential equations [46]-[48]. In general, the parameters in equivalent-circuit models may vary with aging or operating conditions, so impedance must be obtained for different setpoints (SOC, temperature…) to get a complete and good parametrization [46].

A. Thèvenin electric model

This model consists of a voltage source in series with a resistor and an RC branch in parallel. It models the charging and discharging behavior of a battery with simple electric elements as shown in Fig. 1. The voltage source represents the OCV, R_s accounts for the resistance of the contacts, terminals, collectors, electrodes, and electrolyte; and R_d and C_d model the battery transient response, resulting from the effect of diffusion

and charge transportation, in addition to the double-layer capacitance existing between the electrolyte and the active materials [7], [21]. The circuit parameters can be obtained from the voltage response of the battery to a current step.

B. *RC model*

This model consists of a voltage source in series with a resistor and several RC branches in parallel, as shown in Fig. 2, where the voltage source is the OCV; R_s represents the internal resistance; and the parallel branches (i.e. R1||C1, R2||C2, R3||C3) model battery dynamics [43]. This model can be seen as an extension/improvement of the Thévenin model. The number of parallel branches increases the accuracy but also the complexity of the model.

C. *Randles model*

A widely extended methodology for battery characterization is the Electrochemical Impedance Spectroscopy (EIS). EIS-meters apply a sinusoidal AC voltage to the battery; the impedance is obtained from the applied voltage and the resulting current [34], [49]. Fig. 3a shows the EIS results (polar plot) for one sample of the $LiFePO_4$ batteries used in this paper (see Fig. 4). The AC voltage was generated with a Hewlett Packard 33120A waveform generator. Current and voltage waveforms were measured with a Yokogawa 701932 current probe and with a Yokogawa 701938 voltage probe, respectively. Signals were captured with a Yokogawa 701251 16-bit 2 channels module, which is plugged into a Yokogawa DL850 ScopeCoder. The real axis represents the resistance and the imaginary axis the reactance. Each point in the graph corresponds to the impedance at a different frequency; the frequency increases from right to left in the capacitive region, and opposite in the inductive region, as indicated in the figure. The impedance values obtained by the EIS analysis are used to obtain the Randles model [10], [28], [45] equivalent circuit (see Fig. 3b). The lower frequency range is used to obtain Z_W, which represents the Warburg impedance and accounts for the diffusion phenomena and cathode resistance. The middle frequency range is dominated by the parallel RC branch dynamics (in some cases, more than one parallel RC branch is

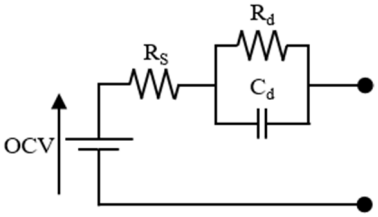

Fig. 1.- Thévenin equivalent model of a battery.

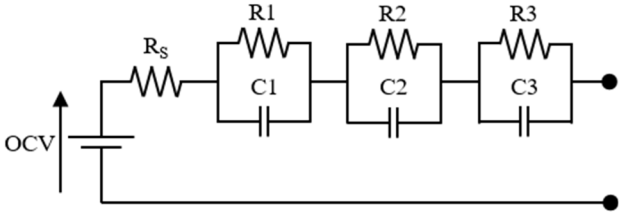

Fig. 2.- Battery model using a third-order RC circuit.

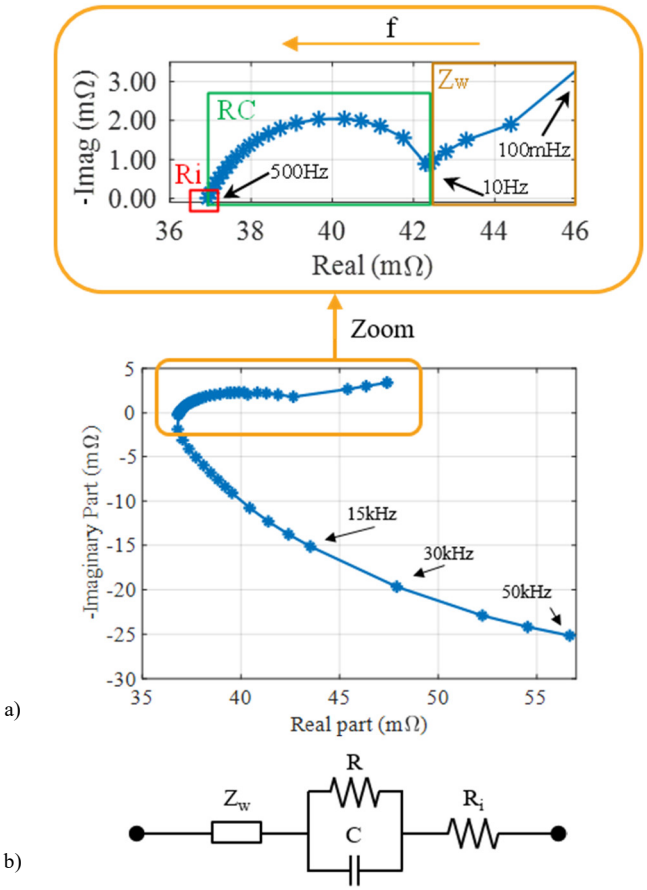

Fig. 3.- a) EIS analysis with a closed detail from the capacitive part. b) Randles equivalent model derived from the EIS analysis.

Fig. 4.- $LiFePO_4$ battery.

used to accurately describe the battery behavior), which corresponds to the electrolyte and SEI resistance on the anode: C represents the double-layer capacitance at the cathode/electrolyte and lithium/electrolyte interface; R is the charge transfer resistance (transfer of Li^+ ions between electrode and electrolyte); and R_i is the resistance of the electrolyte and collector when the battery impedance changes from capacitive to inductive, which corresponds to the intercept frequency [38]. This inductive behavior, which represents the battery collectors and leads, is sometimes represented by a pure inductor in the Randles model but is normally neglected [10]. Although its use is normally restricted to static analysis [34], EIS analysis can also be used for transient impedance estimation during battery charging/discharging [7].

In general, there is not a unique approximation to battery modeling, there are several possibilities involving

combinations of simple electric elements. Among the aforementioned models, EIS is the most common choice for temperature estimation [28], [29], [32]-[40], and more specifically the resistive elements as they are expected to change with the battery temperature. However, model parameters might be also affected by SOC and load; these issues are further discussed in section VII. In addition, there are many applications in which the battery needs a power converter to be driven. The inherent switching harmonics of the power converter will allow the estimation of the battery impedance, see Fig. 3a; all these issues will be discussed in section IV.

IV. Battery control using electronic power converters

Voltage in a battery varies with SOC, being the OCV vs SOC curves dependent on the battery chemistry [13]. $LiFePO_4$ batteries have a flat characteristic for medium SOCs (see Fig. 5). This is an advantage from the user point of view because the voltage variation will be small. In some systems, the admissible DC voltage variation limit is very small, or the required voltage is very high, making unpractical a high number of series-connected cells. In this case, a DC/DC converter between the batteries and the rest of the system to stabilize the DC voltage independently of the battery SOC is required [3], [5]. These converters can also provide galvanic isolation if needed. Examples of converters used for battery integration are Neutral-Point Clamped (NPC) converters, without isolation (for direct coupling), or Dual Active Bridge (DAB), with isolation provided by a high-frequency transformer. They can be found in microgrids or electric vehicles, among other applications [3], [5]. In any of these cases, the converter will generate switching harmonics, which will affect the voltage and current waveform in the battery. The effect of switching harmonics in the batteries is still an open topic for intense research efforts, and limited information is available [50]-[52]. In this paper, the bidirectional boost converter shown in Fig. 6 is used. Table I shows the test setup parameters. The current control loop block diagram of the bidirectional boost converter is shown in Fig. 7, where I_{bat}* is the current command; I_{bat} is the battery current; e_i is the current error signal; V_{bat} is the battery voltage; V_{out} is the power converter output voltage; V_L is the voltage across the inductor; d is the top switch duty cycle; and G(s) represents the plant model, i.e. the battery and converter filter. A Proportional-Integral (PI) controller is used to track the battery current command.

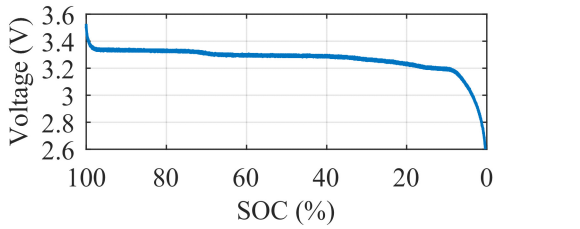

Fig. 5.- SOC curve of a $LiFePO_4$ cell (discharge).

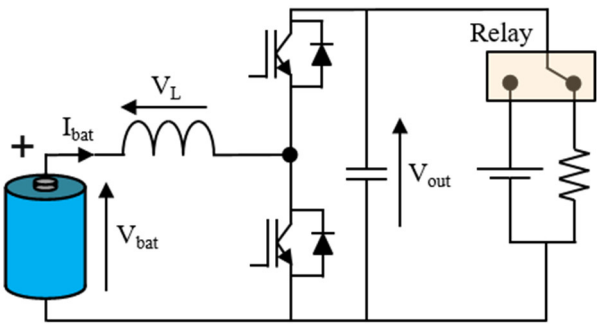

Fig. 6.- Boost converter scheme used to charge and discharge the battery.

V. Battery temperature estimation using switching harmonics

This section presents the proposed battery temperature estimation method using switching harmonics. The switching frequency is set depending on the application and power switch technology, e.g. Mosfet/IGBT, Silicon/Silicon Carbide/Gallium Nitride… Fig. 8 and Fig. 9 show discharging waveforms of the battery current and voltage, respectively, as seen in Fig. 6, and the corresponding frequency spectrums when the battery current command is 2.6 A (discharging current). In addition to the DC component, harmonics at integer multiples of the switching frequency are readily visible in the frequency spectrum. Battery current and voltage can be expressed as (1) and (2) respectively. I_{DC} and V_{DC} are the DC components, I_n and V_n are the magnitudes of the n^{th} switching harmonic of the current and voltage respectively, f_{sw} is the switching frequency, and φ_{Vn} and φ_{In} are the phase angles of the voltage and current n^{th} harmonic respectively. The battery impedance at each frequency can be obtained from any of the harmonic components of the voltage and current (3), where R_{batn} and X_{batn} are the battery resistance and reactance at the frequency of the n^{th} harmonic component. Resistance value at any frequency can be modeled to be a linear function of the battery temperature (4), where R_{batn0} is the battery resistance at the frequency of the n^{th} harmonic component at the room temperature (T_o), T_{bat} is the battery temperature and α_{bat} is the temperature coefficient; R_{batn0} and α_{bat} can be measured during a commissioning process. The battery temperature is finally estimated from (5).

TABLE I: BIDIRECTIONAL BOOST CONVERTER AND BATTERY CHARACTERISTIC PARAMETERS.

Parameter	Value
Switching frequency	15 kHz
Converter inductor	478 µH
Nominal battery voltage	3.2 V
Nominal current	3.2A
Maximum charge current	1C
Maximum discharge current	3C
Battery capacity	3300mAh
MOSFETs nominal voltage	75V
MOSFETs nominal current	56A

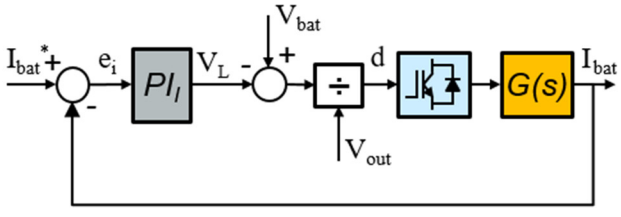

Fig. 7.-Battery current controller.

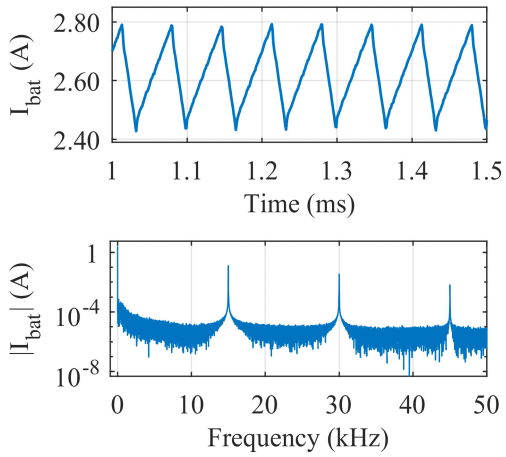

a)

b)

Fig. 8.- a) Battery current, Ibat , and b) FFT of Ibat. Battery discharging @20ºC.

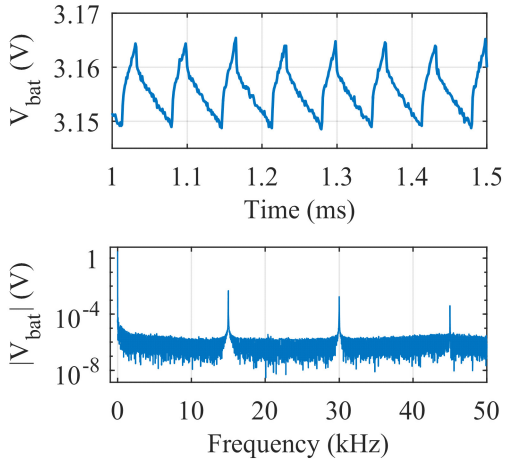

a)

b)

Fig. 9.- a) Battery voltage, V_{bat} , and b) FFT of V_{bat} . Battery discharging @20ºC.

$$I_{bat} = I_{DC} + \sum_n I_n \sin\left(n \cdot 2\pi f_{sw} t + \varphi_{In}\right) \quad (1)$$

$$V_{bat} = V_{DC} + \sum_n V_n \sin\left(n \cdot 2\pi f_{sw} t + \varphi_{Vn}\right) \quad (2)$$

$$Z_{batn} = \frac{V_n \angle \varphi_{Vn}}{I_n \angle \varphi_{In}} = R_{batn} + jX_{batn} \quad (3)$$

$$R_{batn} = R_{batn0}\left(1 + \alpha_{bat}\left(T_{bat} - T_0\right)\right) \quad (4)$$

$$T_{bat} = \frac{R_{batn} - R_{batn0}}{R_{batn0}\alpha_{bat}} + T_0 \quad (5)$$

In this paper, the fundamental component is used to estimate temperature, but other harmonics could be potentially used if necessary, e. g. in case the fundamental switching frequency is not in the inductive region of the battery. The only limitation is the resolution of the Analog to Digital Converter (ADC), as will be seen in section VI. The signal processing block diagram for temperature estimation is shown in Fig. 10. The inputs are the battery current and voltage, both containing the DC fundamental component and the switching harmonics. Two bandpass filters (BPF) are used to isolate the harmonic component at the switching frequency of each signal. These BPFs are adjusted to the frequency of interest, in this case the fundamental component. The battery high-frequency impedance (Z_{batn}) is obtained from (3). The battery high-frequency resistance (R_{batn}) is obtained as the real part of the resulting impedance, and the estimated battery temperature ($\widehat{T_{bat}}$) is finally obtained using (5).

Generally speaking, all methods reviewed in section II ([28], [29], [32]-[40]) show that resistance of the battery decreases as temperature increases. This is explained since the frequencies used to excite the battery in [28], [29] and [32]-[40] are low frequencies in which the effect of the solid electrolyte interface (SEI) [18] and the diffusion processes dominate the battery dynamics in the capacitive region [45]. On the contrary, the switching frequency of power converters are typically in the range of tens/hundreds of kHz; 15 kHz will be used in this paper, meaning that the battery is in the inductive region as seen in the EIS in Fig. 3a. This means that the high-frequency battery impedance is not expected to follow an Arrhenius-like behavior [19] but linear due to the higher impact of the battery collectors and leads on the overall battery impedance in this frequency range [28]. This effect can be seen in Fig. 11, which shows the variation of the internal resistance of the test battery with temperature for two different frequencies: 8 Hz (Fig. 11a) and 15 kHz (Fig. 11b). At 8 Hz, the internal resistance decreases with temperature, as expected [29], [36], but at 15 kHz increases.

It is noted that the proposed method can be used with any switching frequency, as long as the battery is in the inductive region. In addition, enough spectral separation between the fundamental and the switching components must exist in order to properly filter the desired component (see Fig. 10). The range in which the method is valid may vary with the battery type and physical construction. As examples, the batteries used in this

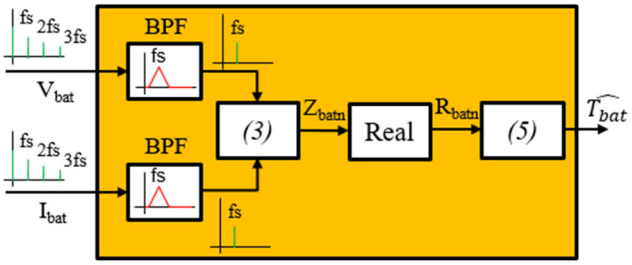

Fig. 10.-Signal processing for battery temperature estimation.

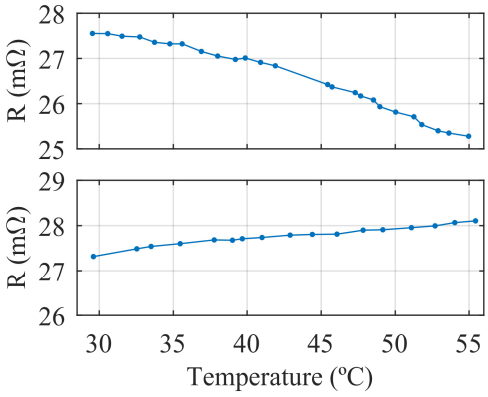

a)

b)

Fig. 11.- Evolution of the battery resistance with temperature applying sinusoidal waveforms (EIS) to the battery at no load: a) 8 Hz frequency, b) 15 kHz frequency.

work show an inductive behavior from 500 Hz (see Fig. 3), while 1.1 kHz is reported in [46].

VI. Implementation issues

A. ADC resolution

Voltage switching harmonic components are significantly smaller than the fundamental component; bit resolution of the data acquisition system is, therefore, a critical implementation issue for the battery characterization. Experimental results shown in Fig. 8 and Fig. 9 were obtained using a 16-bit resolution data acquisition system. Fig. 12 and Fig. 13 show the same results using both 16-bit (1MHz sampling frequency) and 8-bit (4MHz sampling frequency) resolution. These two resolution levels were selected to show the differences between a low- and a high-resolution data acquisition system. It can be observed in Fig. 13 that there is a remarkable difference in the voltage waveform between both cases. It is clearly observed that 8-bit resolution does not provide accurate voltage measurement. The experiments in these figures were carried out at 2.6A of DC discharging current. As it will be demonstrated in section VII-A, there is almost no change in the amplitude of the peak to peak variation of the current with DC current level, so these results are representative for all DC current levels.

Fig. 14 shows the ideal transfer function of an analog to digital converter (solid black). The Least Significant Bit (*LSB*) is the result of dividing the full-scale range (*FSR*) of the acquisition system by the number of discrete values obtained with *n* bits (6). From Fig. 13 it is clear that the maximum quantization error (e_{aa}) is half the *LSB* (7) [53]; the relative error (e_{ar}) being, therefore, the quantization error divided by the amplitude of the signal (*M*) being measured according to (8).

$$LSB = \frac{FSR}{2^n} \tag{6}$$

$$e_{aa} = \frac{LSB}{2} \tag{7}$$

$$e_{ar} = \frac{e_{aa}}{M} \cdot 100 = \frac{LSB}{2M} \tag{8}$$

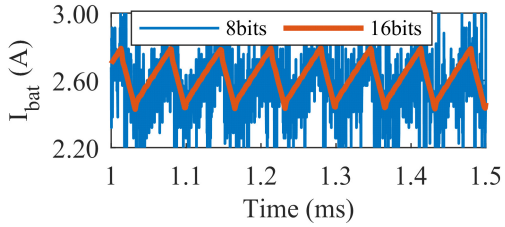

Fig. 12.- Battery current I_{bat}, when measured with an 8 and a 16 bits data acquisition system.

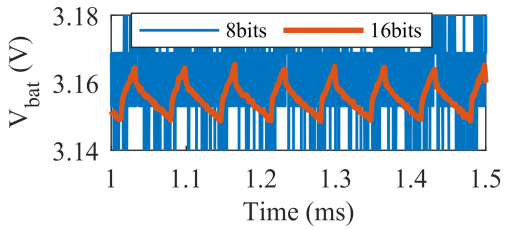

Fig. 13.- Battery voltage, V_{bat}, when measured with an 8 and a 16 bits data acquisition system.

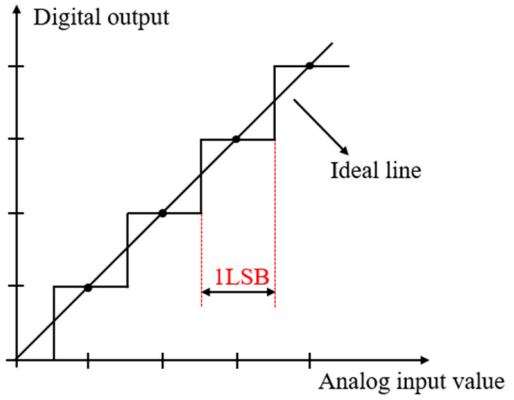

Fig. 14.- Ideal transfer function of an ADC.

Experimental results in Fig. 13 are captured with 5V *FSR*, so applying (6) the *LSB* for the 8-bit case corresponds to 19.53 mV, which is larger than the peak-to-peak amplitude of the triangular waveform in Fig. 9a (14.6 mV); for the 16-bit case, the *LSB* corresponds to 0.076mV. This means it will be difficult to measure the voltage with the 8-bit ADC.

Fig. 15a shows the battery voltage for both the 8-bit and 16-bit case after it has been filtered with a 15 kHz first-order bandpass filter (as a part of the signal processing shown in Fig. 10). As can be seen, the high value of the LSB in the 8-bit case results in an inaccurate and oscillating measurement, while with 16 bits the peak value of the sinusoidal is steady. For clarification, Fig. 15b shows a shorter interval from Fig. 15a, where the peak oscillation in case of 8 bits is clearly noticed.

Fig. 16a shows the relative measurement error (8) in the battery current and voltage for different bit resolutions of the data acquisition system, assuming a voltage level as in Fig. 9a. It is observed that for an 8-bit resolution, the voltage error is ≈ 67%, while for 16-bit resolution is ≈ 0.02%. For the case of the current, the peak-to-peak value at the switching frequency (Fig. 8a) is higher compared to the DC component, so it is not as critical as the voltage, resulting therefore in a smaller error for the same bit resolution (e.g. error with 8-bit resolution is ≈5.5%, while for the voltage is ≈66%). Fig. 16b shows the relative temperature estimation error vs. the bit resolution of the data acquisition system. It can be observed that a bit resolution

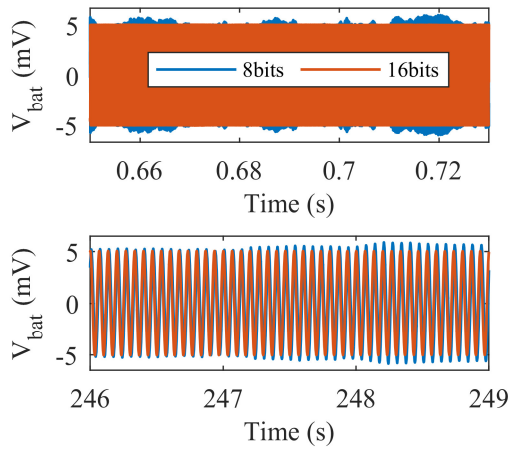

Fig. 15.- a) Filtered voltage in the battery with a BPF at 15 kHz, b) Short interval from a).

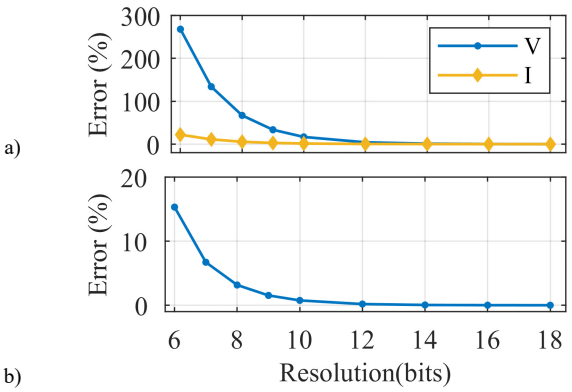

Fig. 16.- Relative measurement error at the switching frequency as a function of the bit resolution of the data acquisition system, a) battery current and voltage magnitude, and b) battery temperature estimation.

greater than 8-bit results in a small relative error, <3%. This is the maximum propagation error of the real part in (3), provided that there is no phase estimation error. Therefore, ADC resolutions commonly found in cost-effective microcontrollers can be employed for this application.

VII. Experimental results

Fig. 17 shows a picture of the power converter in Fig. 6. The battery terminal voltage and current are measured using a 16-bit data acquisition system. According to section VI, any acquisition system with resolutions higher than 8-bit could be used. $LiFePO_4$ battery and IRFU3607 MOSFETs [54] rated parameters are shown in Table I. Actual battery temperature is measured with an LM35 temperature sensor [55], placed in direct contact with the middle of the battery's surface.

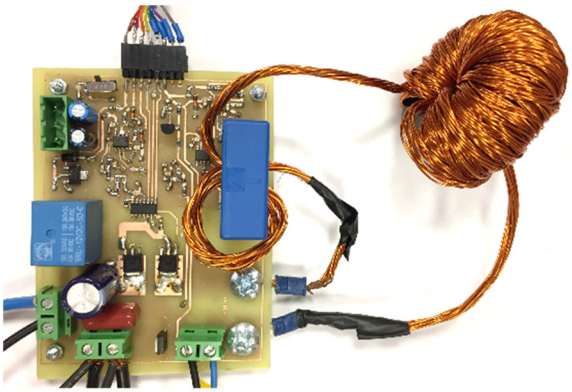

Fig. 17.- Power converter prototype.

Some geometries of batteries, as pouch cells, have a temperature gradient during normal battery operation [56], which results in higher temperatures in the collectors. However, this is not the case of the batteries under test (i.e. cylindrical batteries), see Fig. 18, which is also in good agreement with [57]. This is explained by the construction of the cell, in which the anode and the cathode are rolled up together with a separator on the middle [58]. In batteries where a temperature gradient exists during normal battery operation, the method still can be applied provided that during the commissioning process to estimate α_{bat}, the sensor is in contact with the collector (hottest

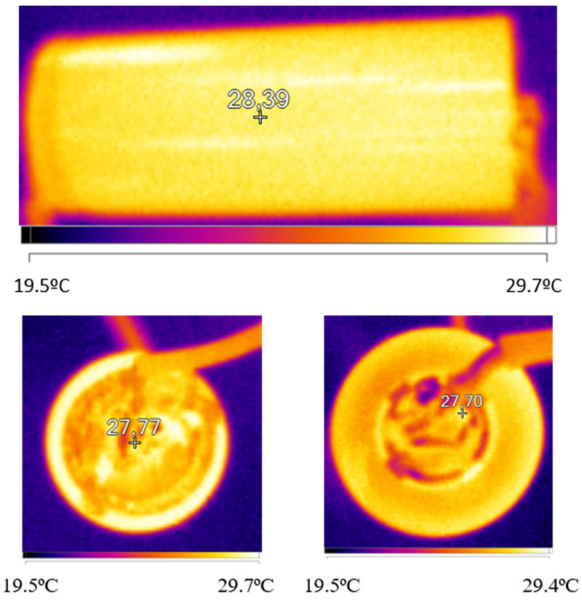

Fig. 18.- Thermal map of the cell during a discharging process; the cell is connected to the converter shown in Fig. 17. Top: cell. Bottom left: negative collector. Bottom right: positive collector. The thermal image is obtained with a Fluke Thermal Imager Ti110.

point), meaning that the estimated temperature will be always the highest one.

A. Resistance variation with SOC

Fig. 19 shows the estimated battery resistance at 15 kHz (switching frequency) vs. discharging DC current for different SOCs and for two $LiFePO_4$ battery samples, B1 and B2, respectively. The battery temperature is kept constant during these experiments. Battery internal resistance at 15 kHz is shown to vary less than 1.7% when the discharging current changes from 0.6 A (0.15C) to 5.6A (1.75C).

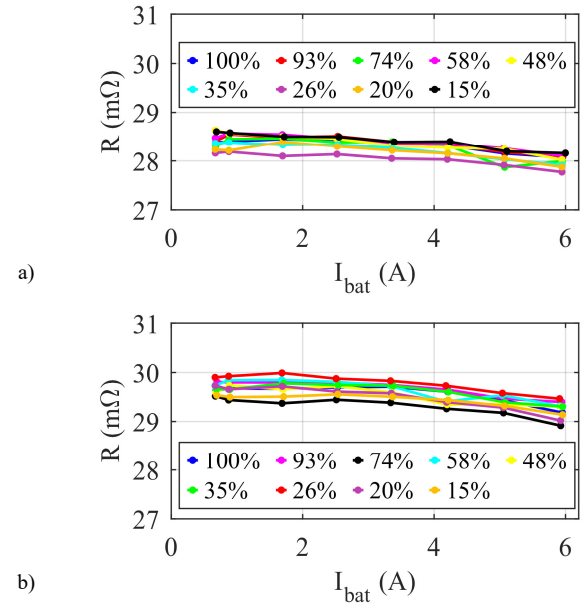

Fig. 19.- Battery resistance (@ 15 kHz) vs. discharging DC current for different SOCs for: a) battery B1; b) battery B2. T=22ºC.

The variation rate of the battery internal resistance with the discharging current is approximately 0.08 mΩ/A, and almost independent of the SOC. Fig. 20 shows the variation of the battery internal resistance with the SOC at 1C discharging rate. It is observed that the battery internal resistance is almost independent of the SOC at the switching frequency (15 kHz).

B. Resistance and reactance variation with temperature

Fig. 21 shows the battery resistance and reactance at the switching frequency vs. the battery temperature for cell B1 in Fig. 19a. The battery temperature was initially heated up to 70ºC; the battery impedance is measured while the battery cools down at room temperature. The converter is only operated for measurement in short periods to avoid battery discharge before the room temperature has been achieved.

Resistance is seen to increase almost linearly with temperature, while the reactance variation does not show a clear trend. As expected from Fig. 11, the resistance increases with temperature, since the switching frequency (15 kHz) is high enough for the battery to be in the inductive region (see Fig. 3a), the battery resistance is dominated by the collector resistance in this region [28]. It is also observed from Fig. 19 and Fig. 21 that resistance variations with SOC are negligible compared to variations due to temperature [32], [34], [37]. In the other hand, DC current levels can be easily compensated, since they follow a linear trend (see Fig. 19). This means that SOC and DC fundamental current are not expected to influence the reliability of the proposed method significantly. These results confirm the validity of the proposed method for battery temperature estimation.

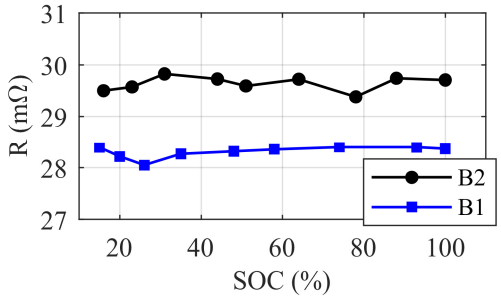

Fig. 20.- Variation of R@15kHz at 3.2 A discharge current with SOC for the two batteries in Fig. 19. T=22ºC.

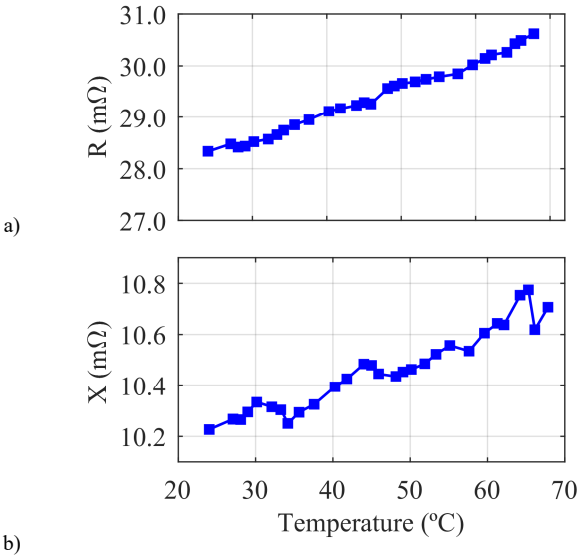

Fig. 21.- a) Battery resistance, and b) reactance, @15 kHz vs. battery temperature. I_{DC}=3.2A.

The experimental results shown in Fig. 21a have been performed in three additional $LiFePO_4$ units (B2, B3 and B4); the results are shown in Fig. 22. These results were obtained following the same procedure as in Fig. 21. It is observed that there is an offset in the internal resistance among cells, however, the rate of variation of the internal battery resistance is almost the same for all batteries. Since the battery temperature will be estimated from the variation of the resistance with temperature respect to the room temperature resistance (R_{batn0}), see (5), offsets among cells are not expected to affect the accuracy of the method.

Fig. 23 shows the measured and estimated temperature using (5); α_{avg} (≈0.0617 1/ºC) being obtained as the average of α_{bat} for the four cells that have been analyzed (see Fig. 22). α_{bat} for each battery can be seen in Table II. This coefficient is obtained from the slope of the linear regression approximating the temperature variation in each battery, which is obtained during a commissioning process. Fig. 24 shows the temperature estimation error for all batteries analyzed in Fig. 23; the temperature estimation error is seen to be less than ≈ 10ºC. This error can be reduced if the calibration is considered for individual batteries but wouldn't be considered practical in most cases.

Fig. 25 shows the temperature estimation error of the proposed method for cells B1and B2 for different discharging current and SOC levels; cell temperatures were kept constant during all experiments. The variation of resistance with different current levels is compensated by means of a look-up Table (LUT), experimentally obtained like Fig. 19, since the resistance decreases evenly with current for every SOC. The reference value for the resistance is taken at 1C current (same level used to obtain all the experimental results in section VII-B). It can be observed that the estimation errors in both cases is less than 5ºC, except for one of the SOC levels in battery 2 (Fig. 25b).

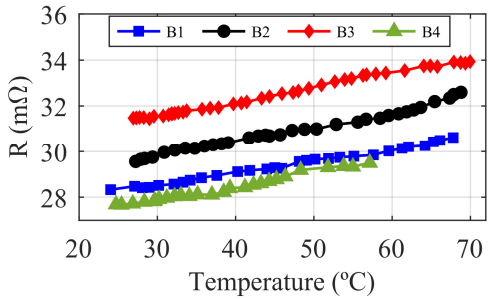

Fig. 22.- Battery resistance (@15 kHz) vs. battery temperature for different batteries. I_{DC}=3.2A.

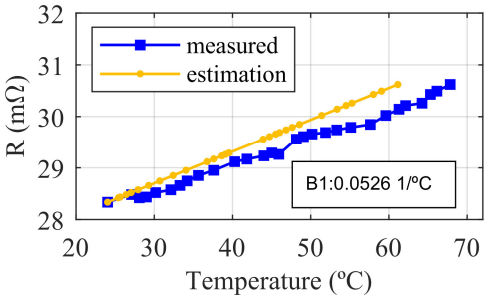

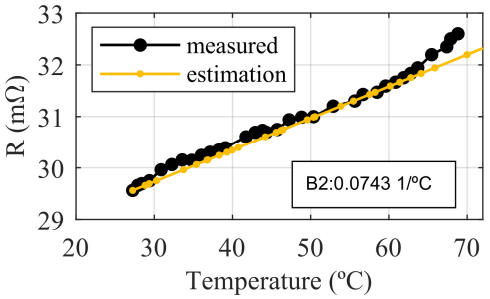

b)

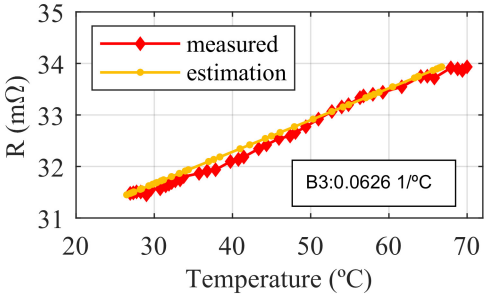

c)

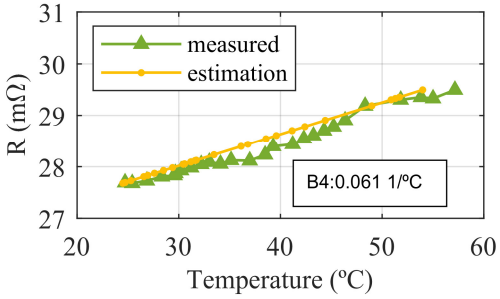

d)

Fig. 23.- Measured and estimated temperatures for four different batteries, a)-d) B1-B4. fsw =15kHz. IDC=3.2A.

TABLE II: THERMAL COEFICIENTS FOR THE DIFFERENT CELLS EVALUATED

Battery	Thermal coefficient α_{bat} (1/ºC)
1 (blue in Fig. 23)	0.0526
2 (black in Fig. 23)	0.0743
3 (red in Fig. 23)	0.0626
4 (green in Fig. 23)	0.0610
Average	0.0617

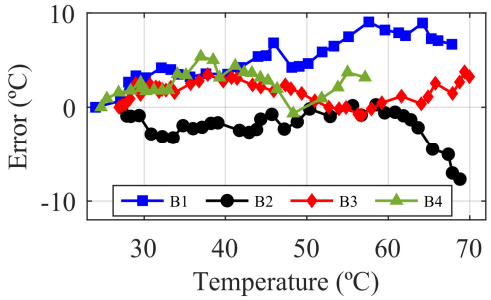

Fig. 24.- Error between measured and estimated temperature. fsw =15kHz, IDC=3.2A.

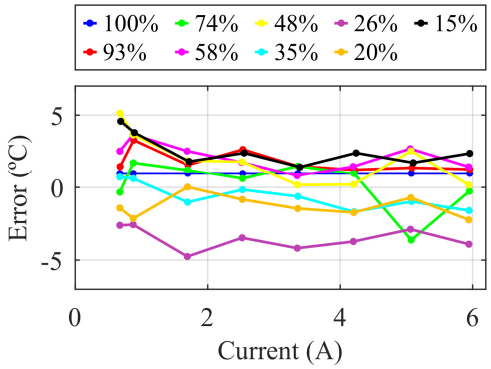

a)

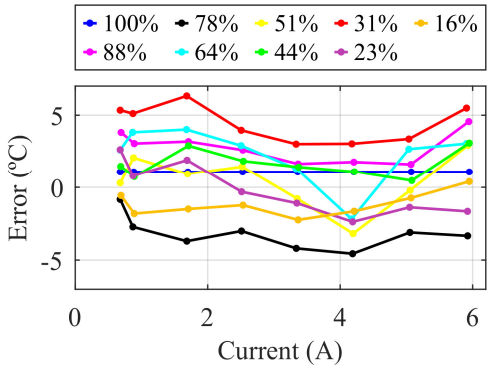

b)

Fig. 25.- Estimation error at 22ºC for batteries in Fig. 19 for different SOCs and current levels. a) cell B1, b) cell B2. T= 22ºC.

VIII. Conclusions

This paper proposes a temperature estimation method for $LiFePO_4$ batteries using switching harmonics produced by the power converter used to feed the battery. Temperature is estimated from the measured battery resistance at the switching frequency. The method allows online temperature monitoring without injecting additional signals and without interfering with the normal operation of the system. It has been shown that the SOC and the discharging DC current do not affect significantly the method reliability and can be easily compensated. Experimental results have been provided to demonstrate the viability of the proposed method.

IX. Acknowledgment

The authors wish to acknowledge the support and motivation provided by the University of Oviedo, Spain and Electrotécnica Industrial y Naval, S.L. (ELINSA), Spain.

X. References

[1] Z. Liao, S. Zhang, K. Li, G. Zhang and T. G. Habetler, "A survey of methods for monitoring and detecting thermal runaway of lithium-ion batteries", Journal of Power Sources, vol. 436, Oct. 2019.

[2] I. Alsaidan, W. Gao and A. Khodaei, "Optimal design of battery energy storage in stand-alone brownfield microgrids," North American Power Symposium (NAPS), Morgantown, WV, pp. 1-6, Sept. 2017.

[3] Z. Miao, L. Xu, V. R. Disfani and L. Fan, "An SOC-Based Battery Management System for Microgrids," IEEE Transactions on Smart Grid, vol. 5, no. 2, pp. 966-973, March 2014.

[4] M. T. Lawder, B. Suthar, P. W. C. Northrop, S. De, C. M. Hoff, O. Leitermann, M. L. Crow, S. Santhanagopalan, V. R. Subramanian, "Battery Energy Storage System (BESS) and Battery Management System (BMS) for Grid-Scale Applications," Proceedings of the IEEE, vol. 102, no. 6, pp. 1014-1030, June 2014.

[5] M. Bragard, N. Soltau, S. Thomas and R. W. De Doncker, "The Balance of Renewable Sources and User Demands in Grids: Power Electronics for Modular Battery Energy Storage Systems," IEEE Transactions on Power Electronics, vol. 25, no. 12, pp. 3049-3056, Dec. 2010.

[6] D. Anseán, M. González, V. M. García, J. C. Viera, J. C. Antón and C. Blanco, "Evaluation of $LiFePO_4$ Batteries for Electric Vehicle Applications," IEEE Transaction on Industrial Application, vol. 51, no. 2, pp. 1855-1863, March-Apr 2015.

[7] M. Einhorn, F. V. Conte, C. Kral and J. Fleig, "Comparison, Selection, and Parameterization of Electrical Battery Models for Automotive Applications," IEEE Transactions on Power Electronics, vol. 28, no. 3, pp. 1429-1437, March 2013.

[8] S. Buller, M. Thele, E. Karden, R. W. D. Doncker, "Impedance-based non-linear dynamic battery modeling for automotive applications," Journal of Power Sources, vol. 113, no. 2, pp. 422-430, Jan. 2003.

[9] A. E. Mejdoubi, H. Gualous, H. Chaoui and G. Alcicek, "Experimental investigation of calendar aging of lithium-ion batteries for vehicular applications," EMC Conference, Turkiye, Ankara, pp. 1-5, Sept. 2017.

[10] M. Sayegh, C. Forgez, T. H. Tran and G. Cherouvrier, "$LiFePO_4$/graphite battery modelling for an aeronautical application," IEEE-ISIE, Buzios, pp. 1278-1283, June 2015.

[11] J.P. Fellner, G.J. Loeber, S.P. Vukson, C.A. Riepenhoff, "Lithium-ion testing for spacecraft applications," Journal of Power Sources, vol. 119–121, pp. 911-913, 2003.

[12] Gianfranco Pistoia, "In Battery Operated Devices and Systems," Elsevier, Amsterdam, 2009.

[13] H. Rahimi-Eichi, U. Ojha, F. Baronti and M. Y. Chow, "Battery Management System: An Overview of Its Application in the Smart Grid and Electric Vehicles," IEEE Industrial Electronics Magazine, vol. 7, no. 2, pp. 4-16, June 2013.

[14] J. Cao, N. Schofield and A. Emadi, "Battery balancing methods: A comprehensive review," IEEE Vehicle Power and Propulsion Conference, Harbin, pp. 1-6, Sept. 2008.

[15] D. Linden and T. Reddy, "Handbook of Batteries," Edition: 3. New York: McGraw-Hill Professional, 2001.

[16] B. Weißhar and W. G. Bessler, "Model-based degradation assessment of lithium-ion batteries in a smart microgrid," International Conference on Smart Grid and Clean Energy Technologies (ICSGCE), Offenburg, pp. 134-138, Oct. 2015.

[17] J. C. Koo, S. K. Lee and S. W. Ra, "Lithium-ion battery design for the hybrid satellite in the geostationary orbit," International Telecommunications Energy Conference (INTELEC), Incheon, pp. 1-6, Dec. 2009.

[18] D. A. González, "High power Li-ION battery performance: A mechanistic analysis of aging." PhD thesis, University of Oviedo, 2015. Available: http://hdl.handle.net/10651/34551 [Accessed: Jan 16th, 2018].

[19] C. D. Rahn and C.-Y. Wang, "Battery systems engineering," Edition: 1. United Kingdom: John Wiley & Sons, Ltd, 2013.

[20] Markets and markets, "Lithium Ion Battery Market - Global Forecast to 2025". Jan. 2019. Available: https://www.marketsandmarkets.com/Market-Reports/lithium-ion-battery-market-49714593.html [Accessed: Oct. 30th, 2019].

[21] M. A. Roscher, D. U. Sauer, "Dynamic electric behavior and open-circuit-voltage modeling of LiFePO4-based lithium ion secondary batteries," Journal of Power Sources, vol. 196, pp. 331-336, Jan. 2011.

[22] AA Portable Power Corp, "LiFePO4/LiFeMnPO4 Batteries". Available: https://www.batteryspace.com/LiFePO4/LiFeMnPO4-Batteries.aspx [Accessed: Jan 16th, 2018].

[23] F. Feng, R. Lu, G. Wei and C. Zhu, "Identification and analysis of model parameters used for LiFePO4 cells series battery pack at various ambient temperature," IET Electrical Systems in Transportation, vol. 6, no. 2, pp. 50-55, May 2016.

[24] M. Takahashi, S. Tobishima, K. Takei, Y. Sakurai, "Reaction behavior of $LiFePO_4$ as a cathode material for rechargeable lithium batteries," Solid State Ionics, vol. 148, no. 3–4, pp. 283-289, June 2002.

[25] L. W. Juang, P. J. Kollmeyer, T. M. Jahns and R. D. Lorenz, "Improved modeling of lithium-based batteries using temperature-dependent resistance and overpotential," IEEE-ITEC, Dearborn, MI, pp. 1-8, June 2014.

[26] ENIX Energies, "Specification Approval Sheet," ACL9012 -3.3Ah datasheet. Document number S470XLB029. Apr 2012. Version A0.

[27] Q. Wang, P. Ping, X. Zhao, G. Chu, J. Sun, C. Chen, "Thermal runaway caused fire and explosion of lithium ion battery," Journal of Power Sources, vol. 208, pp. 210-224, June 2012.

[28] N. S. Spinner, C. T. Love, S. L. Rose-Pehrsson, S. G. Tuttle, "Expanding the Operational Limits of the Single-Point Impedance Diagnostic for Internal Temperature Monitoring of Lithium-ion Batteries," Electrochimica Acta, vol. 174, pp. 488-493, August 2015.

[29] R. Srinivasan, B. G. Carkhuff, M. H. Butler, A. C. Baisden, "Instantaneous measurement of the internal temperature in lithium-ion rechargeable cells," Electrochimica Acta, vol. 56, no. 17, pp. 6198-6204, July 2011.

[30] C. Alaoui, "Solid-State Thermal Management for Lithium-Ion EV Batteries," IEEE Transactions on Vehicular Technology, vol. 62, no. 1, pp. 98-107, Jan. 2013.

[31] K. Zaghib, K. Striebel, A. Guerfi, J. Shim, M. Armand, M Gauthier, "LiFePO4/polymer/natural graphite: low cost Li-ion batteries," Electrochimica Acta, vol. 50, pp. 263-270, Nov 2004.

[32] R. R. Richardson, P. T. Ireland, D. A. Howey, "Battery internal temperature estimation by combined impedance and surface temperature measurement," Journal of Power Sources, vol. 265, pp. 254-261, Nov. 2014.

[33] R. Schwarz, K. Semmler, M. Wenger, V. R. H. Lorentz and M. März, "Sensorless battery cell temperature estimation circuit for enhanced safety in battery systems," Annual Conference of the IEEE Industrial Electronics Society (IECON), Yokohama, pp. 001536-001541, Nov. 2015.

[34] J.G. Zhu, Z.C. Sun, X.Z. Wei, H.F. Dai, "A new lithium-ion battery internal temperature on-line estimate method based on electrochemical impedance spectroscopy measurement," Journal of Power Sources, vol. 274, pp. 990-1004, Jan. 2015.

[35] J.G. Zhu, Z.C. Sun, X.Z. Wei, H.F. Dai, "Battery Internal Temperature Estimation for LiFePO4 Battery Based on Impedance Phase Shift under Operating Conditions," Energies, vol. 10, pp. 1-17, Jan. 2017.

[36] R. Srinivasan, "Monitoring dynamic thermal behavior of the carbon anode in a lithium-ion cell using a four-probe technique," Journal of Power Sources, vol. 198, pp. 351-358, Jan. 2012.

[37] J. P. Schmidt, S. Arnold, A. Loges, D. Werner, T. Wetzel, E. Ivers-Tiffée, "Measurement of the internal cell temperature via impedance: Evaluation and application of a new method," Journal of Power Sources, vol. 243, pp. 110-117, Dec. 2013.

[38] L.H.J. Raijmakers, D.L. Danilov, J.P.M. van Lammeren, M.J.G. Lammers and P.H.L. Notten, "Sensorless battery temperature measurements based on electrochemical impedance spectroscopy," Journal of Power Sources, vol. 247, pp. 539-544 , Feb. 2014

[39] L. H. J. Raijmakers, D. L. Danilov, J. P. M. V. Lammeren, T. J. G. Lammers, H. J. Bergveld and P. H. L. Notten, "Non-Zero Intercept Frequency: An Accurate Method to Determine the Integral Temperature of Li-Ion Batteries," IEEE Transactions on Industrial Electronics, vol. 63, no. 5, pp. 3168-3178, May 2016.

[40] R. R. Richardson and D. A. Howey, "Sensorless Battery Internal Temperature Estimation Using a Kalman Filter With Impedance Measurement," IEEE Transactions on Sustainable Energy, vol. 6, no. 4, pp. 1190-1199, Oct. 2015.

[41] J. A. A. Qahouq and Z. Xia, "Single-Perturbation-Cycle Online Battery Impedance Spectrum Measurement Method With Closed-Loop Control of Power Converter, " IEEE Transactions on Industrial Electronics, vol. 64, no. 9, pp. 7019-7029, Sept. 2017.

[42] C. G. Moral, D. Fernandez, J. M. Guerrero, D. Reigosa and F. Briz, "Thermal monitoring of LiFePO4 batteries using switching harmonics," IEEE Energy Conversion Congress and Exposition (ECCE), Portland, OR, pp. 2734-2740, Sept. 2018.

[43] R. Ahmed, "Modeling and state of charge estimation of electric vehicle batteries." PhD thesis, McMaster University, 2014.

[44] C. Birkl and D. Howey, “Model identification and parameter estimation for LiFePO4 batteries,” IET Hybrid and Electric Vehicles Conference (HEVC), London, pp. 1-6, Nov. 2013.
[45] Y. F. Pulido, C. Blanco, D. Anseán, M. González, J. C. Viera and V. M. García, “Effect of aging on C/LFP battery impedance: Operating conditions to which the impedance has minimal variations,” IEEE International Conference on Environment and Electrical Engineering and IEEE Industrial and Commercial Power Systems Europe (EEEIC / I&CPS Europe), Milan, pp. 1-5, June 2017.
[46] J. Kowal, J. B. Gerschler, C. Schäper, T. Schoenen and D. U. Sauer, “Efficient battery models for the design of EV drive trains,” International Power Electronics and Motion Control Conference (EPE-PEMC) , Ohrid, Macedonia, pp. S11-31-S11-38, Sept. 2010.
[47] J. Newman, K. E. Thomas, H. Hafezi and D. R. Wheeler, “Modeling of lithium-ion batteries,” Journal of Power Sources, vol. 119–121, pp. 838-843, June 2003.
[48] L. Gagneur, A.L. Driemeyer-Franco, C. Forgez, G. Friedrich, “Modeling of the diffusion phenomenon in a lithium-ion cell using frequency or time domain identification,” Microelectronics Reliability, vol. 53, no. 6, pp. 784-796, June 2013.
[49] Digatron Power Electronics, “Electrochemical Impedance Spectroscopy EIS-Meter”. Available: http://www.digatron.com/en/cells-packs/ . [Accessed: Jan 17th, 2018].
[50] R. Soares, A. Bessman, O. Wallmark, G. Lindbergh and P. Svens, “Measurements and analysis of battery harmonic currents in a commercial hybrid vehicle,” IEEE Transportation Electrification Conference and Expo (ITEC), Chicago, IL, pp. 45-50, June 2017.
[51] F. Savoye, P. Venet, M. Millet and J. Groot, “Impact of Periodic Current Pulses on Li-Ion Battery Performance,” IEEE Transactions on Industrial Electronics, vol. 59, no. 9, pp. 3481-3488, Sept. 2012.
[52] K. Uddin, A. D. Moore, A. Barai, J. Marco, “The effects of high frequency current ripple on electric vehicle battery performance,” Applied Energy, vol. 178, pp. 142-154, Sept. 2016.
[53] B. Widrow, I. Kollar and M. C. Liu, “Statistical theory of quantization,” in IEEE Transactions on Instrumentation and Measurement, vol. 45, no. 2, pp. 353-361, Apr. 1996.
[54] Infineon, IRFR3607PbF datasheet, Apr. 2010.
[55] Texas Instruments, LM35 Precision Centigrade Temperature Sensors datasheet, Aug. 1999. Revised Dec. 2017.
[56] B. Wu, Z. Li, y J. Zhang, “Thermal Design for the Pouch-Type Large-Format Lithium-Ion Batteries I. Thermo-Electrical Modeling and Origins of Temperature Non-Uniformity”, Journal of the Electrochemical Society, vol. 162, no. 1, pp. A181-A191, Jan. 2015.
[57] P. Chanthevee, S. Hirai, V. Lailuck, Y. Laoonual, P. Siriam, S. Rompho, N. Chanurai and M. Masomtob, "A Simplified Approach for Heat Generation Due to Entropy Change in Cylindrical LCO Battery," *2018 IEEE Transportation Electrification Conference and Expo, Asia-Pacific (ITEC Asia-Pacific)*, Bangkok, 2018, pp. 1-5.
[58] J. Matthey, “Automotive Lithium-Ion Batteries - Developments for passenger car applications”, Johnson Matthey Technology Review, vol. 59, no. 1, pp. 4-13, 2015.